

MaRS: Mars Express Orbiter Radio Science

M. Pätzold¹, F.M. Neubauer¹, L. Carone¹, A. Hagermann¹, C. Stanzel¹, B. Häusler², S. Remus², J. Selle², D. Hagl², D.P. Hinson³, R.A. Simpson³, G.L. Tyler³, S.W. Asmar⁴, W.I. Axford⁵, T. Hagfors⁵, J.-P. Barriot⁶, J.-C. Cerisier⁷, T. Imamura⁸, K.-I. Oyama⁸, P. Janle⁹, G. Kirchengast¹⁰ & V. Dehant¹¹

¹*Institut für Geophysik und Meteorologie, Universität zu Köln, D-50923 Köln, Germany*

Email: paetzold@geo.uni-koeln.de

²*Institut für Raumfahrttechnik, Universität der Bundeswehr München, D-85577 Neubiberg, Germany*

³*Space, Telecommunication and Radio Science Laboratory, Dept. of Electrical Engineering, Stanford University, Stanford, CA 95305, USA*

⁴*Jet Propulsion Laboratory, 4800 Oak Grove Drive, Pasadena, CA 91009, USA*

⁵*Max-Planck-Institut für Aeronomie, D-37189 Katlenburg-Lindau, Germany*

⁶*Observatoire Midi Pyrenees, F-31401 Toulouse, France*

⁷*Centre d'etude des Environnements Terrestre et Planetaires (CETP), F-94107 Saint-Maur, France*

⁸*Institute of Space & Astronautical Science (ISAS), Sagamihara, Japan*

⁹*Institut für Geowissenschaften, Abteilung Geophysik, Universität zu Kiel, D-24118 Kiel, Germany*

¹⁰*Institut für Meteorologie und Geophysik, Karl-Franzens-Universität Graz, A-8010 Graz, Austria*

¹¹*Observatoire Royal de Belgique, B-1180 Bruxelles, Belgium*

The Mars Express Orbiter Radio Science (MaRS) experiment will employ radio occultation to (i) sound the neutral martian atmosphere to derive vertical density, pressure and temperature profiles as functions of height to resolutions better than 100 m, (ii) sound the ionosphere to derive vertical ionospheric electron density profiles and a description of the ionosphere through its diurnal and seasonal variations with solar wind conditions; MaRS will also (iii) determine the dielectric and scattering properties of the martian surface in target areas by a bistatic radar experiment, (iv) determine gravity anomalies for the investigation of the structure and evolution of the martian crust and lithosphere in conjunction with observations of the High Resolution Stereo Camera as a base for 3D topography, and (v) sound the solar corona during the superior conjunction of Mars with the Sun.

The radio carrier links of the spacecraft Telemetry, Tracking and Command subsystem between the Orbiter and Earth will be used for these investigations. Simultaneous and coherent dual-frequency downlinks at X-band (8.4 GHz) and S-band (2.3 GHz) via the High Gain Antenna will permit separation of contributions from the classical Doppler shift and the dispersive media effects caused by the motion of the spacecraft with respect to the Earth and the propagation of the signals through the dispersive media, respectively.

The investigation relies on the observation of the phase, amplitude, polarisation and propagation times of radio signals transmitted from the spacecraft and received with antennas on Earth. The radio signals are affected by the medium through which they propagate (atmospheres, ionospheres, interplanetary medium, solar corona), by the gravitational influence of the planet on the spacecraft and, finally, by the performances of the various systems aboard the spacecraft and on Earth.

1. Introduction

Initially conceived as an exploratory tool, radio-science techniques have provided considerable knowledge of the atmospheres and gravity of the planets – much of it unexpected. Previous experiments at Mars have demonstrated accuracies in measurements of martian atmospheric surface pressure and temperature that surpassed those of *in situ* measurements made with the Viking Landers (Hinson et al., 2001). This performance can be matched or possibly improved for occultation immersion measurements with Mars Express.

Radio-science techniques are applied to the study of planetary and cometary atmospheres, planetary rings and surfaces, gravity and the solar corona. Much of our current knowledge of these subjects is based on radio-science observations. Early investigations include the Mariner, Pioneer and Viking missions, as well as Soviet projects. Recent and current experiments involve Voyager (Eshleman et al., 1977; Tyler, 1987), Ulysses (Bird et al., 1994; Pätzold et al., 1995), Giotto (Pätzold et al., 1991a; 1991b; 1993), Galileo (Howard et al., 1992), Magellan (Tyler et al., 1991) and Mars Global Surveyor (Tyler et al., 2001). Planned experiments include Cassini (Kliore et al., 2002), Cassini-Huygens (Bird et al., 1995), Rosetta (Pätzold et al., 2000) and Mars Express.

Radio-science investigations fall into three broad categories: propagation, bistatic radar and gravity. First, when the trajectory of the spacecraft takes it behind the planet as seen from Earth, there is occultation by the planet's atmosphere. A radio signal propagating from the spacecraft to a ground station travels through the ionosphere and neutral atmosphere before being blocked by the planetary surface. This sequence is reversed upon emergence of the spacecraft. During an occultation event, the refractive index of the gases in the ionosphere and atmosphere alter the characteristics of the propagating radio wave. The method can be extended to any one of several separable 'atmospheres', including planetary rings and magnetospheres, as well as the relativistic gravitational effects of stars (Eshleman, 1973). In conducting such observations, the geometry and other experimental conditions must be controlled so that the only significant unknown factors are the properties of the medium along the radio path.

Second, oblique incidence scattering investigations using propagation paths between spacecraft, planetary surface and Earth station can be used to explore the surface properties through the microwave scattering function. The technique was first described by Fjeldbo (1964). It is referred to as 'bistatic radar' because the transmitter and receiver are separated by significant angular distances or ranges. The first such experiment in space was conducted with Luna-11 in August 1966 to study the Moon's surface (Yakaovlev & Efimov, 1966). The oblique scattering geometry afforded by Lunar Orbiter-1, in October 1966, provided the signal source for the first US experiment (Tyler et al., 1967). Signals from Explorer-35 also contained echos from the lunar surface (Tyler, 1968a). Fortuitously, the plane of the spacecraft spin axis and the antenna polarisation made it possible to measure the Brewster angle of the lunar crust, leading to an unambiguous value for the relative dielectric constant of lunar soil of between 2.9 and 3.1, confirming that landers would be on firm ground.

Third, when the radio path is well clear of occulting material, the spacecraft can be treated as a classical 'test particle' falling in the gravity field of the planetary system. This type of experiment is optimised when the component of its velocity is along the line-of-sight to the tracking station, thus allowing a measurement of the Doppler effect. The spacecraft motion causing the Doppler shift is in response to the variations in mass distribution within a planet or its satellites. This is a classical physics laboratory experiment carried out at planetary-scale. Our global knowledge of Earth's gravity field comes from such studies. The only information on the gravity field of Mercury is based on the two flybys of Mariner-10 (Anderson et al., 1987). Similarly, recent observational inferences on the internal structures of the Galilean satellites (for example, that there is an ocean on Europa) are based on the perturbations of Galileo's trajectory during close flybys (Anderson et al., 1992; 1997). A precise determination of the total mass of Uranus and Neptune from the Voyager-2 flybys (Tyler et al., 1986)

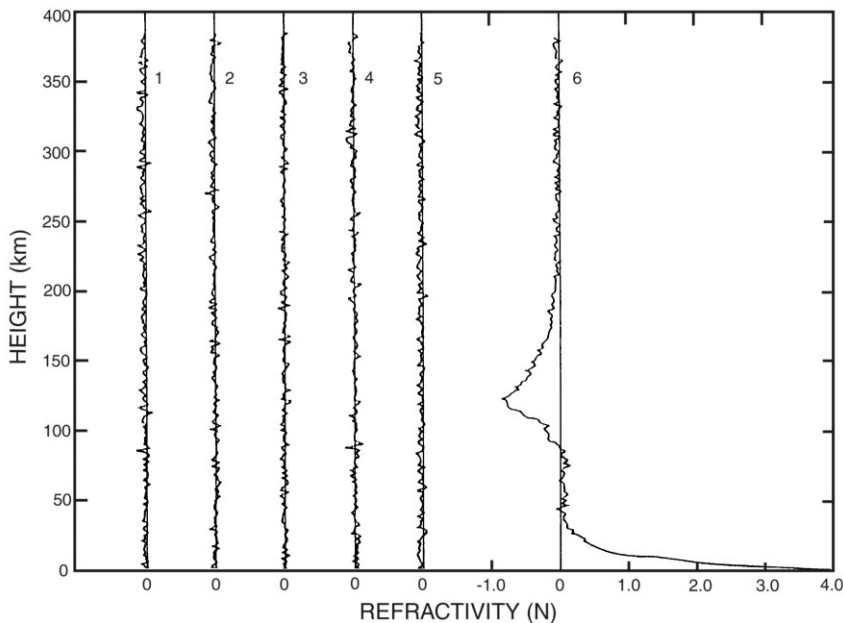


Fig. 1. Refractivity profiles at S-band obtained from the Mariner-4 occultation. Profiles 1-5 were taken prior to the occultation and represent the zero level after biases and trends owing to effects not connected with the martian atmosphere were removed. Profile 6 shows the refractivity of the martian atmosphere at S-band probed during occultation entry. Negative refractivity represents the ionosphere, positive the neutral atmosphere (from Fjeldbo & Eshleman, 1968).

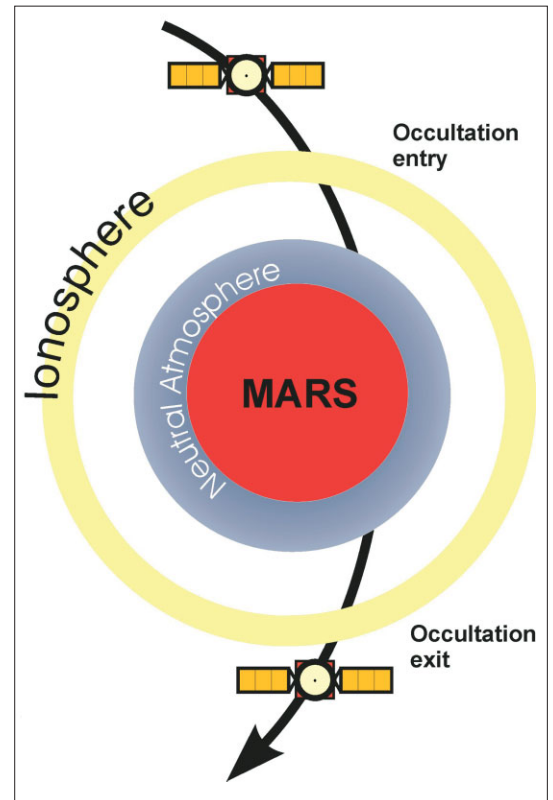


Fig. 2 (right). Operational sequence for the use of the two-way link for sounding the atmosphere/ionosphere as seen from the Earth. The sequence is seen projected on to the plane of the sky. The two-way radio ray slices through the atmosphere from the top to the surface during occultation entry and is then shadowed by the planet. After leaving occultation, the now one-way ray slices through the atmosphere from the surface to the upper levels of the ionosphere, where the two-way radio link may be reestablished.

has led to the conclusion that there is no need for a 'Planet X' to explain the orbits of these bodies (Standish, 1993). The method has been extended to small bodies, such as the mass determination of asteroid Mathilde (Yeomans et al., 1997) and the gravity field of asteroid Eros (Yeomans et al., 2000), and is planned for the Rosetta flyby at asteroid Siwa in 2008 (Pätzold et al., 2001). For Mars Express, these asteroid techniques can be applied to precise determinations of the masses of Phobos and Deimos during close encounters.

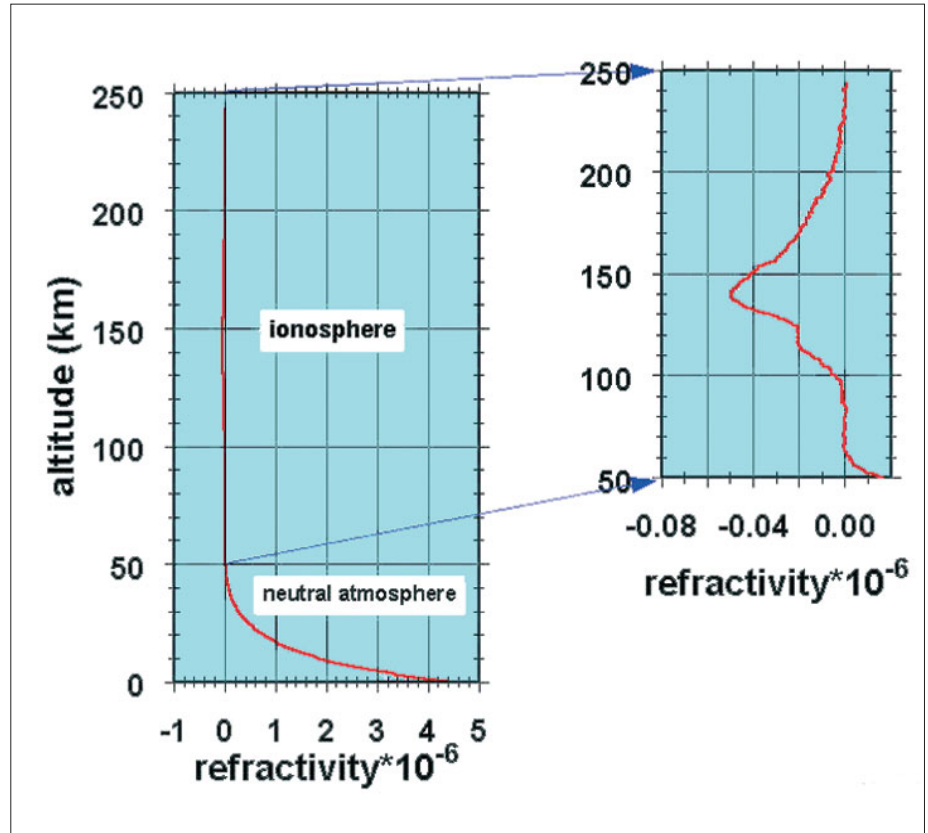
2.1 Radio sounding of the neutral atmosphere and ionosphere

The modern value for the surface pressure of Mars was first determined in 1965 by using the radio occultation method with Mariner-4 (Kliore et al., 1965). Prior to that, the literature indicated a consensus that the surface pressure was of the order 100 mbar (about 10% of Earth's), based on spectroscopic observations from the ground, with many believing that oxygen was a likely major constituent.

A more accurate value was needed in support of martian landers being studied by NASA teams lead by Wehrner von Braun. At the time of the Mariner-4 launch and cruise, new ground-based observations of the atmosphere had begun to cast doubt on the 100 mbar value, suggesting that the true value could be substantially lower. As a result, Mariner-4 was directed to fly behind Mars to perform radio occultation measurements. Initial results showed the surface pressure at the occultation point was approximately 4 mbar (Fig. 1). Further, since spectrographic studies indicated that the partial pressure of CO₂ on Mars was in this range, the atmosphere was almost entirely carbon dioxide with little, if any, oxygen. Radio occultation measurements have been included on almost all planetary missions flown since.

2. Science Objectives

Fig. 3. X-band refractivity profile obtained with Mars Global Surveyor on 11 March 1999. Note that the positive refractivity is comparable to that shown in Fig. 1 at S-band. The inset shows on a larger scale the negative refractivity of the ionosphere. The peak refractivity translates into a peak electron density of 8.7×10^{10} electrons m^{-3} . Ionospheric refractivity at X-band scales by a factor of $(3/11)^2$ relative to that at S-band in Fig. 1.



Sounding by radio occultation of Mars Express (Fig. 2) will contribute to the understanding of the structure of the martian atmosphere, its circulation and dynamics through the day and seasons. Vertical profiles of density, pressure and temperature with height resolutions better than 100 m can be derived. Observations of the vertical structure below 30 km altitude have been made by several spacecraft during occultations. *In situ* measurements of three atmospheric profiles during the descents of the two Viking landers and Pathfinder are available below 200 km altitude. Dust and haze in the atmosphere do not hinder the propagation of the radio carrier waves, but the local heating by entrained dust is observed in several occultation temperature profiles. The Mars Global Surveyor (MGS) radio occultation experiment (Tyler et al., 1992) retrieved vertical profiles of pressure and temperature extending from the surface to the 10 Pa level, with surface uncertainties of 2 Pa and 1K (Hinson et al., 1999).

Radio occultation also provides a measure of the ionosphere's vertical structure and an averaged large-scale electron density profile as a function of height and planetary latitude at each occultation point. One of the goals is to understand the global behaviour of the martian ionosphere with the effects of the magnetic field, solar activity and solar wind interaction through the day and seasons.

Photochemical processes control the behaviour of the main ionospheric layer in a manner similar to the terrestrial F layer (Barth et al., 1992). The electron density distribution of a weakly magnetised body like Mars is controlled by solar radiation and the solar wind interaction with the planet. A typical value of the daytime ionospheric peak density is of the order of 10^{11} electrons m^{-3} at altitudes of 110-135 km (Fig. 3).

Observations by MGS have revealed highly variable and localised magnetic fields (Acuna et al., 1998). Strong fields at the spacecraft orbit below the ionosphere were

observed locally. At other locations, much weaker magnetic fields were found. Therefore, the possibility of a sufficiently strong global magnetic field involved in the solar wind interaction might no longer be supported. However, only a narrow latitude range was covered by MGS observations owing to the low pericentre altitude during aerobraking.

On the other hand, the radio occultation data from Mariner-9 and Viking (Kliore, 1992) suggest the presence of a global magnetic field in the formation of the ionosphere. With its better resolution (about 100 electrons cm^{-3}), Mars Express may address the question of whether the Mariner/Viking profiles reflect only their low resolution or if a global magnetic field is indeed involved. The height of the ionopause is not well defined at Mars. At Venus, the ionopause has been defined as that altitude where the electron density falls below 500 electrons cm^{-3} (Kliore & Luhmann, 1991), while the density in the martian profiles never drops below that limit. Mars Express needs to solve the question of which physical processes define the ionopause altitude.

Either the entry or the exit of the Mars Express occultations will be at nighttime, providing the opportunity to investigate the nightside ionosphere. Viking resolved a nighttime ionosphere in only 40% of the measurements, which also showed a high variability in shape, peak density and height. The anticipated accuracy of Mars Express will help to solve the question of whether the nighttime ionosphere is maintained by horizontal transport from the dayside or by impact ionisation owing to electron precipitation from the tail, which should provide insights into the direction of the magnetic field on the nightside.

During occultation ingress, the Telemetry, Tracking and Command (TT&C) subsystem will operate in the two-way mode. The spacecraft downlink frequencies are derived from the uplink, stabilised by a hydrogen maser in the ground station. Changes in the received radio frequency (RF) to a fractional frequency stability of 10^{-14} over 3-100 s integration times correspond to a change in the angle of refraction of radio rays in occultation experiments of the order 10^{-8} rad (Tyler, 1987).

The signal-to-noise limitations of previous experiments limited the detectability of the atmosphere to below 30 km. Mars Express should improve this altitude to 50 km because of the high signal-to-noise ratio at X-band (transmitted RF power 65 W). The effective vertical resolution through use of the Abel transform is determined by the first Fresnel zone radius $(\lambda D)^{1/2}$, which is about 300 m for X-band and 600 m for S-band, respectively, (D is the distance of the spacecraft to the closest approach of the ray path to the planet). This resolution is far superior to what can be achieved by other passive sounding instruments, which are limited to typically one atmospheric scale height (order of km).

Marouf et al. (1986) developed a procedure to improve the resolution beyond the natural diffraction limit, applying it to the Voyager occultation by Saturn's rings. Gresh et al. (1989) applied the procedure to occultation data from the rings of Uranus. This resulted in a resolution of 100 m, about an order of magnitude improvement on the Fresnel diffraction limit, for flyby conditions at the outer planets. The technique was also applied in the first direct determination of Triton's surface pressure (Tyler et al., 1989). Karayel & Hinson (1997) applied a similar approach to atmospheres denser than Triton's and produced a resolution of about 40 m for simulated martian conditions. These results justify the expectation that it is feasible to derive vertical profiles in the martian atmosphere with a height resolution better than 100 m.

Separating the effects from the ionosphere and neutral atmosphere on the radio link is feasible by using (a) a dual-frequency downlink, (b) the opposite sign of the refractive index if the radio signal propagates in ionised or neutral media, and (c) the fact that the peak heights of the ionosphere and the detectable neutral atmosphere are well separated. This is demonstrated in Figs. 1 and 3 which show the refractivity profile derived from Mariner-4 occultation data (profile 6) at S-band and a refractivity profile from MGS at X-band, respectively, as a function of height. Negative refractivity results from the ionised plasma in the ionosphere and is proportional to the electron number density; positive refractivity is a property of the neutral

Fig. 4a. Duration of Mars Express occultations (in minutes) over the mission. There will be six occultation seasons (OCP1 to OCP6), with an Earth occultation in each orbit over the expected mission duration of two Martian years.

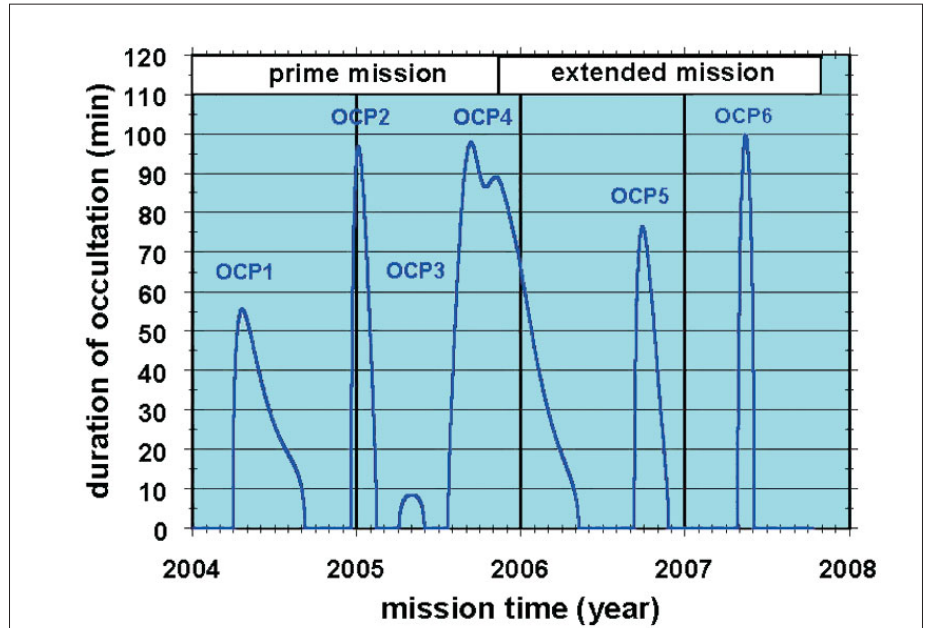
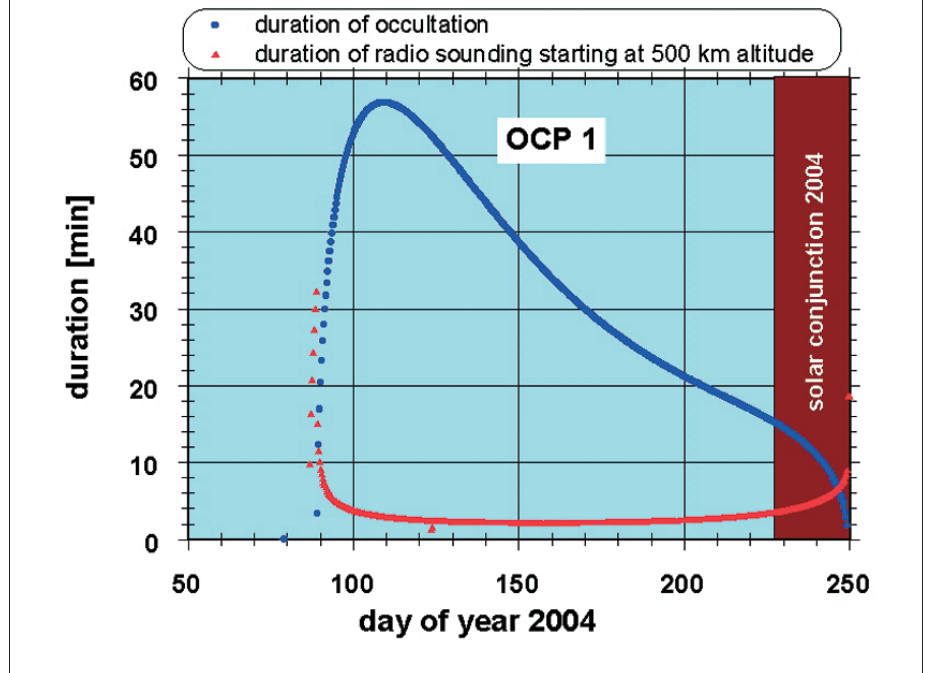


Fig. 4b. Duration of occultations by the planet body during the first season OCP1 (blue dots) and the duration of occultation by the atmosphere between 500 km altitude to the surface (red triangles). The end of the first occultation season is affected by the start of the superior solar conjunction of the planet at year day 238, 2004.



atmosphere which is linearly related to the mass density of the atmospheric constituents (Fjeldbo & Eshleman, 1968). The refractivity μ of free electrons is given by

$$\mu = - 40.31 \times 10^6 \frac{N_e}{f^2}$$

which allows conversion of refractivity into electron number densities (N_e in electrons m^{-3} is the electron density, f in Hz is the radio carrier frequency).

It is feasible to retrieve two refractivity profiles with Mars Express for each radio

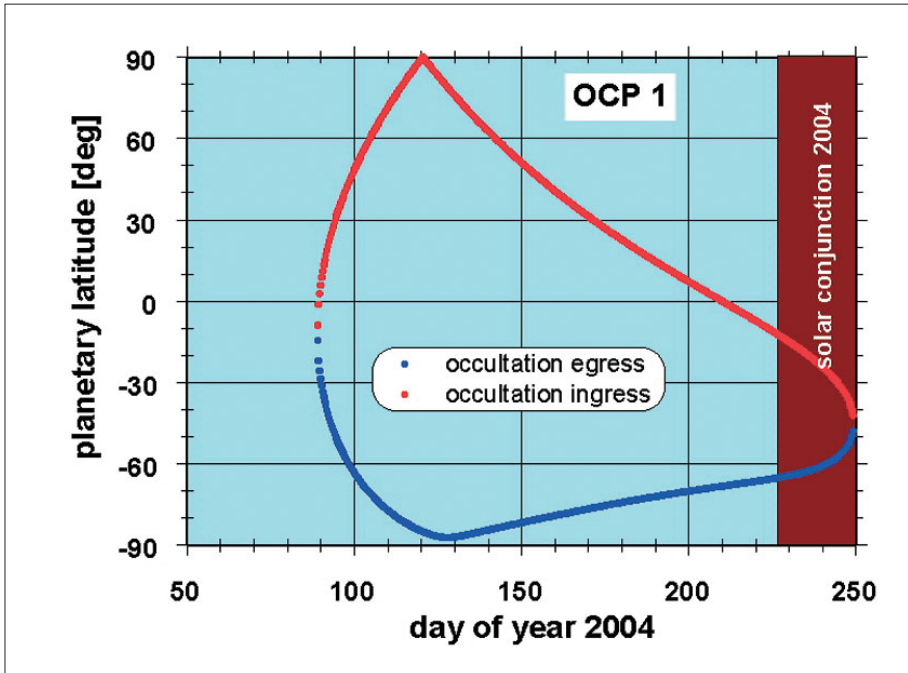


Fig. 5. Spacecraft position along the orbit at occultation entry (red) and occultation exit (blue) for OCP1 expressed as true anomaly. True anomaly of 0 deg is the pericentre position. The red area marks ± 60 deg true anomaly when the spacecraft is nominally in nadir pointing. Occultation can be observed only when ground coverage is available, typically every third occultation.

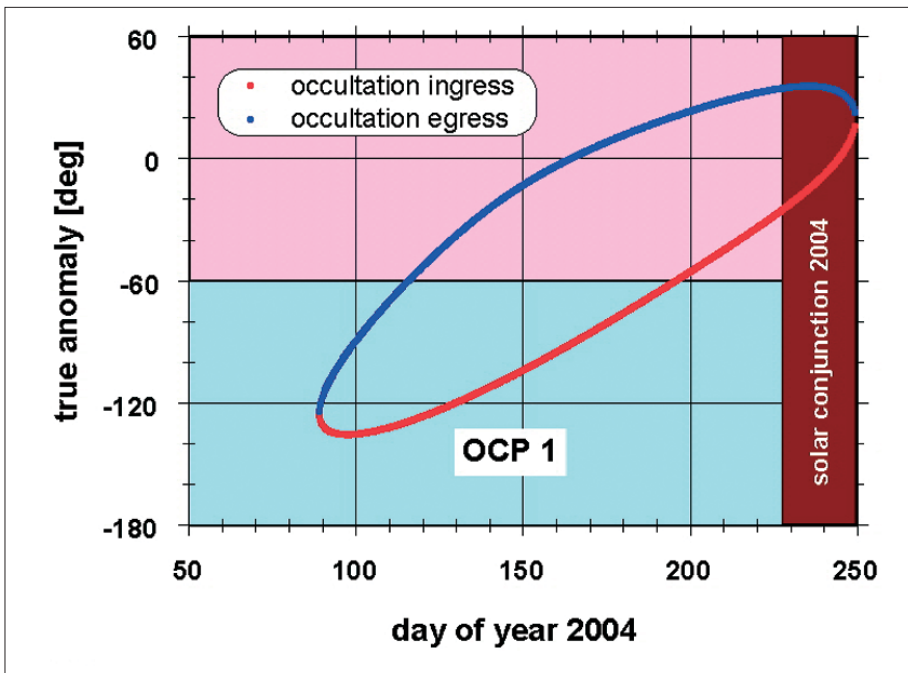


Fig. 6. Planetary latitude of occultation ingress and egress locations during OCP1. Effectively, all planetary latitudes are covered during all six occultation seasons.

carrier frequency at S-band and X-band. S-band is expected to be more sensitive to the negative refractivity (ionosphere) by a factor $(11/3)^2$ compared with X-band, while the positive refractivity (neutral atmosphere) is essentially independent of the frequency. Under favourable geometric conditions it will be possible to investigate the solar wind-magnetic anomalies-ionospheric interaction region.

Computing the differential Doppler from the received S-band and X-band residual Doppler shifts yields the dispersive media effects associated with free electrons in all ionised media (martian ionosphere, interplanetary medium, Earth ionosphere) along the downlink and can be used for calibration, inversion and correction of the classical Doppler shift. The spacecraft-Earth radio ray path will cross through the sensible

ionosphere quickly (in minutes) before entering occultation. The variation in the Earth ionosphere and the interplanetary medium is assumed to be slow for time scales shorter than a minute, so the observed changes in radio carrier properties are assumed to be dominated by the martian ionosphere.

Earth occultations will occur in six ‘seasons’ in the expected 4 years (two martian years) of operation, with one occultation in each orbit or three to four occultations per day. The mission baseline calls for one ground station tracking pass per day, which would cover typically one occultation (two under favourable operational conditions). The duration of the occultation and the entry and exit position of the spacecraft in its orbit expressed in true anomaly are shown in Figs. 4a/4b and Fig. 5, respectively. The occultation entry and exits will cover all planetary latitudes of the northern and southern hemispheres (Fig. 6).

2.2 Determination of the dielectric properties of the surface (bistatic radar)

The bistatic radar configuration (Fig. 7) is distinguished from the monostatic by spatial separation of the transmitter (on the spacecraft) and the receiver (in the ground station on Earth). It may be used to derive information about surface roughness and slope at scales of the incident wavelength (a few cm). Bistatic radar may also be used to determine properties of the surface material, such as dielectric constant, through differential reflection of orthogonal polarisations. The bistatic radar geometry of an orbiting spacecraft is well suited to probing the surface of planets at a variety of latitude, longitude and incidence angles. Bistatic radar experiments have been conducted at the Moon (e.g. Tyler & Howard, 1973; Nozette et al., 1996), Mars (Simpson & Tyler, 1981; Simpson et al., 1984) and Venus (Pettengill et al., 1997; Kolosov et al., 1979).

The objectives at Mars focus on the polar regions and caps, the volcanic regions and the famous ‘Stealth’ area south-west of Tharsis (Muhleman et al., 1991; Edgett et al., 1997). The bistatic geometry is well-suited to probing icy surfaces, which are poorly understood on Mars. The fact that the residual south polar cap on Mars has anomalously high backscatter when viewed from Earth, while the northern cap (presumably much more massive) does not stand out, is a continuing mystery. The Stealth region is anomalous in the sense that it yields very weak backscatter when probed from Earth. In both cases, the unique geometry of a bistatic experiment promises a better understanding of both the scattering processes and the underlying surface geology. Selected targets in other areas, such as volcanic plains, will also be studied. Despite similar appearances in orbital images, some plains do not necessarily have the same radar behaviour, again suggesting differences in the underlying surface geology.

For a typical bistatic radar experiment, the radio signal is transmitted from the spacecraft High Gain Antenna (HGA) towards the surface of Mars and is scattered from the surface. Optimising the performance of these bistatic radar experiments requires accurate prediction of the orbiter trajectory in order to formulate antenna pointing strategies as well as to predict signal parameters such as Doppler shift and signal amplitude. In a quasi-specular experiment, the antenna is programmed to follow the locus of points for which surface reflection would be specular if Mars were smooth. From the data recorded along these specular point paths, surface roughness can be inferred from Doppler dispersion of the echo signal; the dielectric constant ϵ of the surface material can be inferred from echo amplitude and/or polarisation properties. Dielectric properties of a lunar basin were obtained by measuring the Brewster angle $\tan^2\phi_B = \epsilon$ (Tyler, 1968b). Similarly, a more general Stokes parameter analysis led to detection of a tellurium-like material in the Venus highlands (Pettengill et al., 1996).

In a spotlight experiment, the antenna is programmed to track a fixed point on the surface, viewing it from a variety of angles. When the configuration passes through the backscatter geometry, coherent backscatter enhancements can be sought in the echo amplitude and polarisation (Hapke, 1990). Clementine spotlight data have been

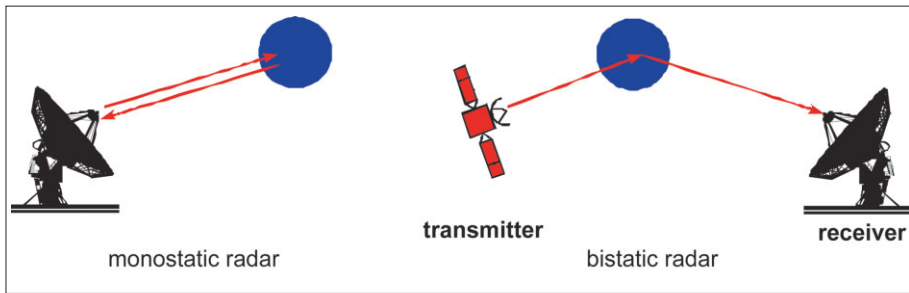


Fig. 7. Bistatic radar configuration is distinguished from the monostatic by the spatial separation of the transmitter (spacecraft) and the receiver (ground station on Earth).

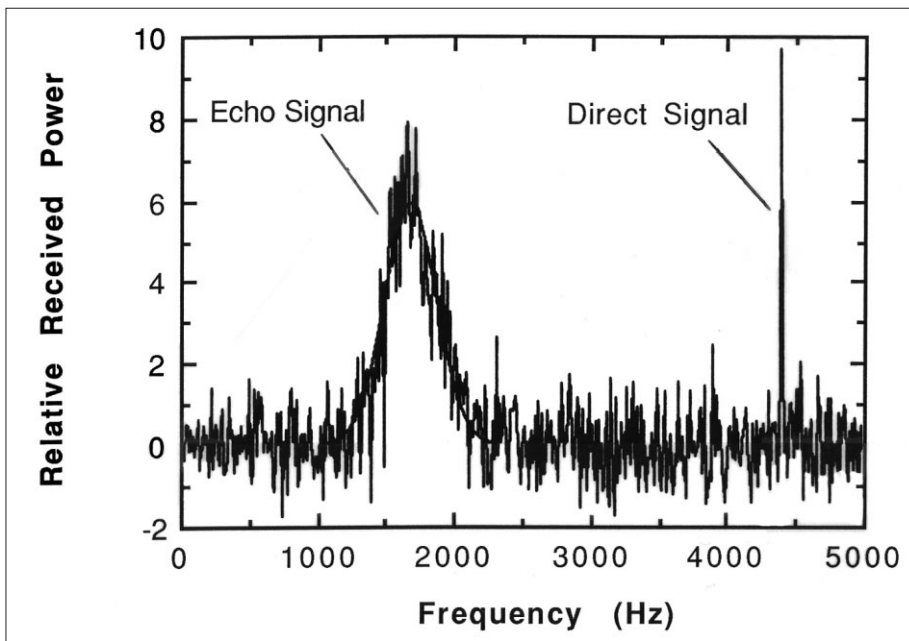


Fig. 8. Typical bistatic radar spectrum showing separation of the echo signal from the direct signal leaking out from the HGA side lobes toward the receiver. The broadening of the echo signal is caused by motion of the specular point over the surface and is related to surface roughness (from Simpson, 1993).

interpreted as suggesting the presence of water ice near the lunar south pole (Nozette et al., 1996; 2001), although that conclusion is not universally accepted (Simpson & Tyler, 1999). Strong backscatter enhancements are the salient features of backscatter from the icy Galilean moons of Jupiter (Eshleman, 1987) and have also been observed in the terrestrial environment of Greenland. Both the mechanism and its expected signature from real targets remain the subjects of active debate (Hagfors et al., 1985; Eshleman, 1987; Peters, 1992). Careful measurement of any observed enhancement magnitude and its angular variation are not available but would be useful.

The radio echo signal is received in the open-loop mode (see below) in two orthogonal polarisations (e.g. Left Circular Polarisation, LCP, and Right Circular Polarisation, RCP), down-converted, sampled and stored for further processing at the investigator's home institution. Fig. 8 shows a typical frequency spectrum of the received radio signal. The direct signal, leaking out from the side lobes of the HGA and reduced accordingly in power, is on the right. The echo signal is on the left and it is Doppler shifted relative to the direct signal according to the change in spacecraft-to-surface-to-Earth distance as a function of time. It is broadened according to the roughness of the surface and the motion of the specular point over the surface (Simpson, 1993).

It is required that the HGA points towards the martian surface. To ensure maximum signal-to-noise ratio in the echo signal received at Earth, the transmission of an unmodulated carrier at the highest feasible power level is also required. Transmission of linear (or elliptical) polarisation offers advantages in detecting differential quasi-

specular polarisation reflections from volcanic plains, while circular (or elliptical) polarisation is preferred for spotlight observations of ice deposits.

2.3 Geophysics: gravity anomalies

The gravity field of a planet is the result of its internal mass distribution and rotational state. Rapidly rotating planets bulge at the equator as a result of centrifugal forces. Consequently, the associated redistribution of mass to the equatorial plane results in a stronger gravitational acceleration of a spacecraft when it is near the pole than when it is at the same altitude located over the equator. Similarly, anomalies in the internal distribution of mass are expressed as departures of the external gravitational field from that of a uniform sphere or a stratified spherical distribution. Space probes in the vicinity of planetary bodies follow trajectories that deviate from the ideal orbits described by Kepler's two-body laws in response to these gravity anomalies.

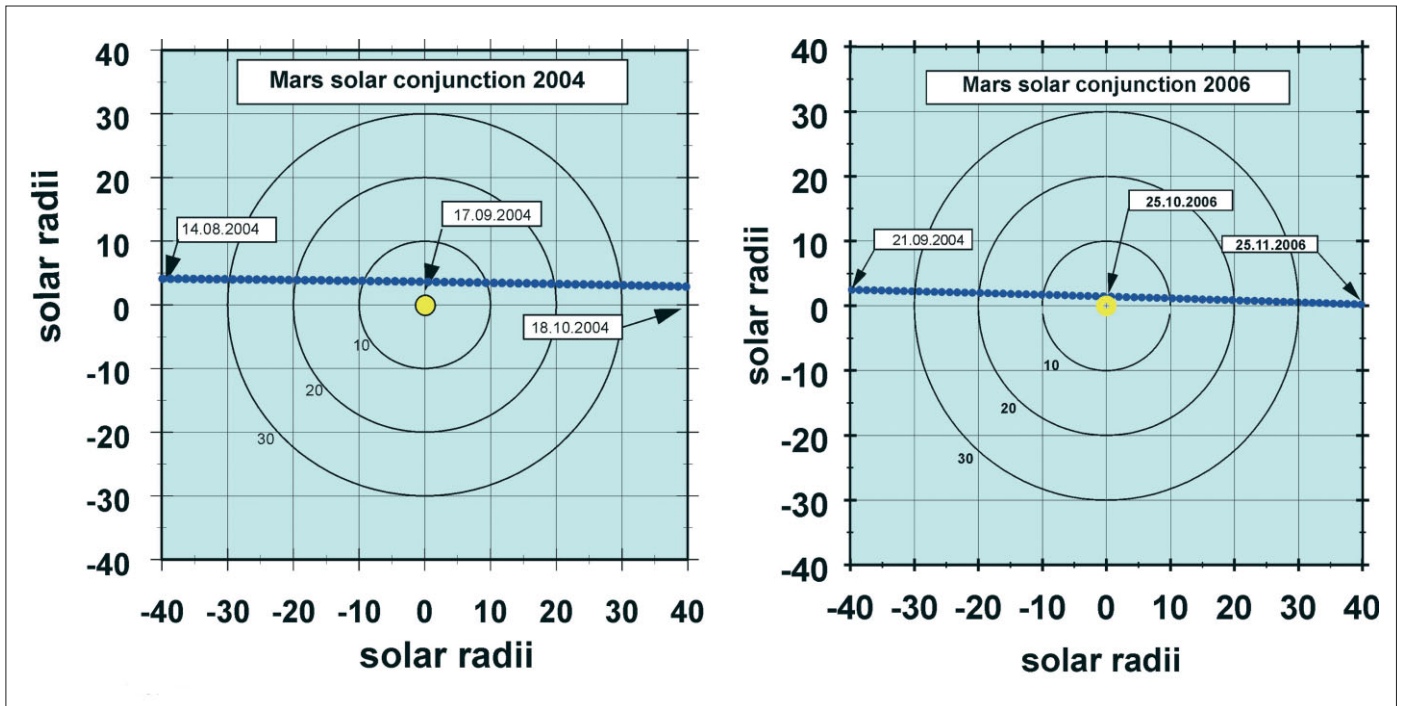
Precision two-way radio tracking provides an accurate measurement of spacecraft velocity along the line-of-sight to the tracking station, with variations attributed to gravitational acceleration owing to mass distribution in the planetary body. The utility of data for studying mass variations depends on the sensitivity of the radio system, the details of the geometry, and the characteristics of the overall spacecraft trajectory. The method is capable of detecting accelerations of the order of 10^{-3} Gal ($1 \text{ Gal} = 10^{-2} \text{ m s}^{-2}$; Earth surface gravity is 982 Gal). Such data, through the connection between mass and gravitational force, are used to study planetary interiors. From low altitudes, even relatively minor variations in the mass density of surface and near-surface features are detectable. For example, a reduction in density of about 300 kg m^{-3} (or about a 10% change in the average martian crustal density) of a 50-km cube of rock near the surface is readily measurable.

Combining data from a large number of orbits from the Mariner, Viking and MGS missions has allowed construction of a complete gravity map, with resolution elements of about 2° on the martian surface. Large-scale variations in the strength of gravity correspond to the overall distribution of mass, mostly in the deep interior of Mars, and are relevant to the interpretation of the early history and evolution of the planet. Smaller scale variations, on lateral distances of a few thousand km or less, correspond to mass variations relatively close to the surface. Both large- and small-scale variations must be interpreted in light of the known overall shape of the planet and the variations in the surface elevation since, as in the examples above, topographic and mass density variations can play a similar role in the raw gravity data. Mars Express, as a result of its low periapsis altitude, can improve the present maps by a factor of about two in linear resolution in areas scanned by the evolution of the orbit.

Two gravity field models of degree and order 50 have been derived from radio tracking data of the Viking and Mariner-9 missions (Smith et al., 1993; Konopliv & Sjogren, 1995). The same teams collaborated on a derivation of a gravity field model of degree and order 60 and higher using the Mars Global Surveyor tracking data (Smith et al., 1999; Yuan et al., 2001).

The highly eccentric orbit of Mars Express is not best-suited for a global investigation of the gravity field. The investigation proposed here focuses on specific target areas for the determination of local gravity anomalies. Observations with the HRSC stereo camera will yield the high-resolution 3D topography of the target area. Three data sets (radio science, camera, radar) will be combined to study the state and evolution of the martian crust and lithosphere, with implications for studying the tectonic evolution of Mars.

The targets of investigations are the hot spot areas of Tharsis and Elysium, large single volcanoes, large impact craters and basins, and the highland-lowland boundary. The investigation of impact basins must be seen in the context of similar studies on other planetary bodies, including the Earth, in the sense of comparative planetology and studies of the impact mechanism, which is not fully understood (particularly for



large basins). Studies of the highland-lowland boundary will contribute to the open question of this dichotomy.

Topographic data provide digital terrain models (DTMs) which, in combination with the gravity data, are the basis for crustal density models. The measured line-of-sight free-air gravity anomaly at spacecraft altitudes amounts up to 70 mGal (Janle & Erkul, 1991). A complete density model consists of a topographic model (DTM) and a density model of the subsurface structures (e.g. undulations of the crust/mantle boundary, mantle plume). Variations in gravity of up to about 500 mGal are associated with topography and drive the need for precise and high-resolution topographic data. DTMs are also necessary for bending-stress models of the lithosphere, as demonstrated by Janle & Jannsen (1986) for Olympus Mons.

Precise DTMs are required for the lithospheric load of bending-stress models, in particular for the correlation of the lineament distribution with the topography and calculated stresses. The combination of radar altimeter data and stereo images from HRSC will provide DTMs with vertical resolutions of 12-18 m and linear ground resolutions of 20-30 m, which are perfectly suited for bending stress models and geologic interpretations of the lineament distribution.

The expected accuracy of the Mars Express X/X-band two-way radio link is of the order $\ll 100 \text{ mm s}^{-1}$ at 10 s integration time. This translates into an accuracy of gravity accelerations of the order of several mGal, depending on the size and extension of the local topographic features (Tyler et al., 1992).

2.4 Radio sounding of the solar corona

Mars will move into superior conjunction with the Sun in the autumns of 2004 and 2006. Within about 10° elongation with respect to the solar disc in the plane of the sky (Fig. 9), the dispersive effects on the radio signals (propagation time, Doppler shift and Doppler noise) are dominated by the solar corona. It is therefore proposed that this valuable time be used for a thorough investigation of the solar corona to derive electron density profiles in the structured corona, solar wind speed, turbulence spectra in the source regions of fast and slow solar wind streams from coronal holes and streamers, respectively, and to detect, identify and describe the spatial and

Fig. 9. Superior solar conjunction geometry of Mars in the plane-of-sky. Each tick mark represents one day. Mars is within 40 solar radii (circles) from 14 August 2004 to 18 September 2004 (left panel), and from 21 September 2006 to 25 November 2006 (right panel). Within 12 solar radii, telemetry reception will be degraded. No telemetry can be expected within 4 solar radii. An adequate signal-to-noise radio carrier can be received at any time, however.

Fig. 10. The Mars Express radio subsystem. The transponder is redundant and each unit contains an S-band and X-band receiver and transmitter. X-band is amplified by TWAs to an RF power output of 65 W. The RF distribution unit (RFDU) connects the receivers and transmitters with the antennas. It also contains the S-band amplifiers (5 W RF power output). The HGA receives uplink at either X-band or S-band and radiates simultaneously X-band and S-band downlink. The LGAs receive and transmit at S-band only.

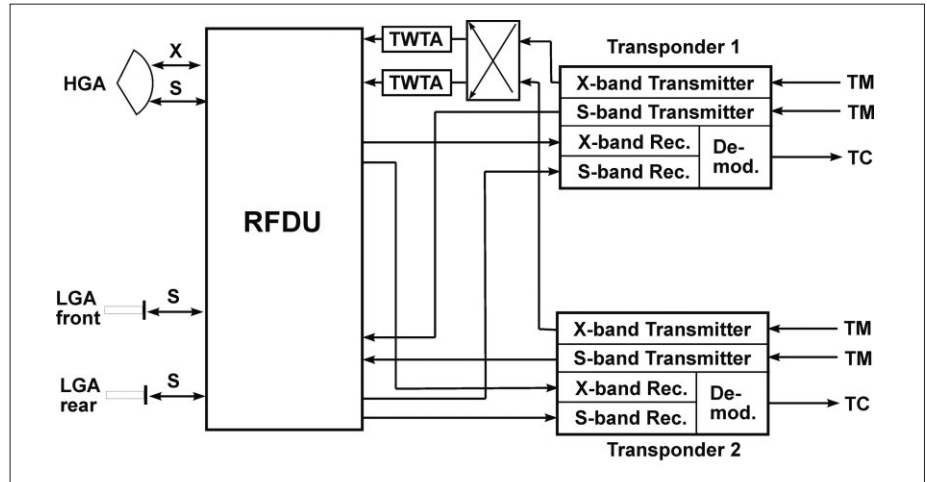
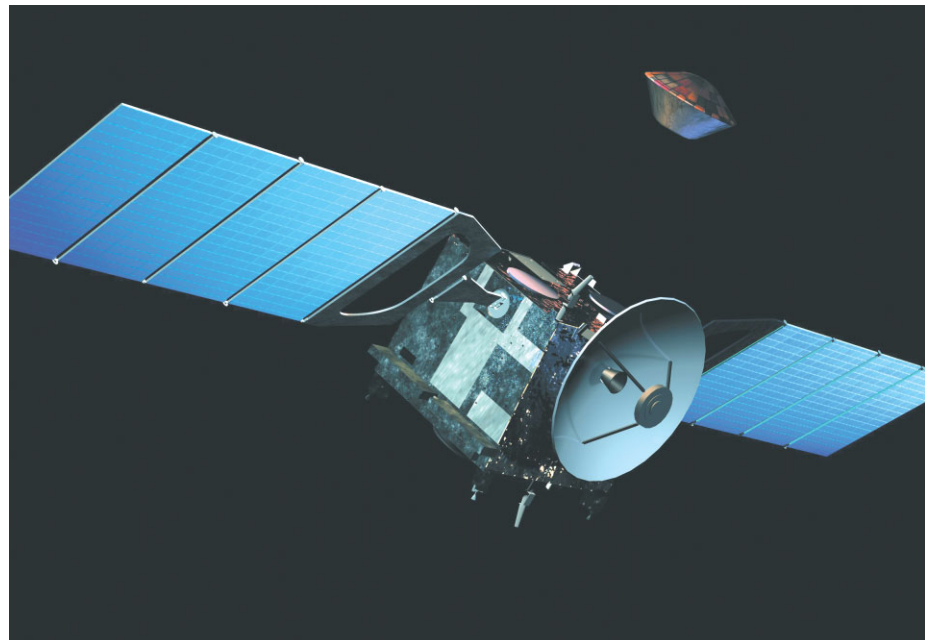


Fig. 11. Mars Express at the time of the release of the Beagle 2 lander descent capsule, showing the fixed HGA, a parabolic dish of 1.60 m diameter. (ESA)



temporal evolution of the shockfronts of coronal mass ejections (Bird et al., 1994; Pätzold et al., 1995; 1996; 1997; Karl et al., 1997). It is highly desirable to carry out these observations simultaneously with SOHO or other solar space observatories to enhance and compare the observations.

The technique of coronal sounding is well established and has been performed by members of the Mars Express team during the superior solar conjunctions of Ulysses (1991, 1995), Magellan (1992), Voyager and Viking (Bird et al., 1992; 1994; 1996; Pätzold et al., 1995; 1996; 1997; Tyler et al., 1977). For Mars Express, a two-way radio link and dual-frequency downlink at S-band and X-band allow separation of the coronal dispersive effects from the classical Doppler shifts. The two-way link is a powerful tool for the derivation of electron density models from observed electron content when propagation time delay, ranging data and dispersive Doppler shifts are compared (Pätzold et al., 1997). Furthermore, it provides the basis for the determination of solar wind speed by correlating uplink and downlink signals (Wohlmuth et al., 1997) and detection of fast outward-propagating density enhancement originating from solar events.

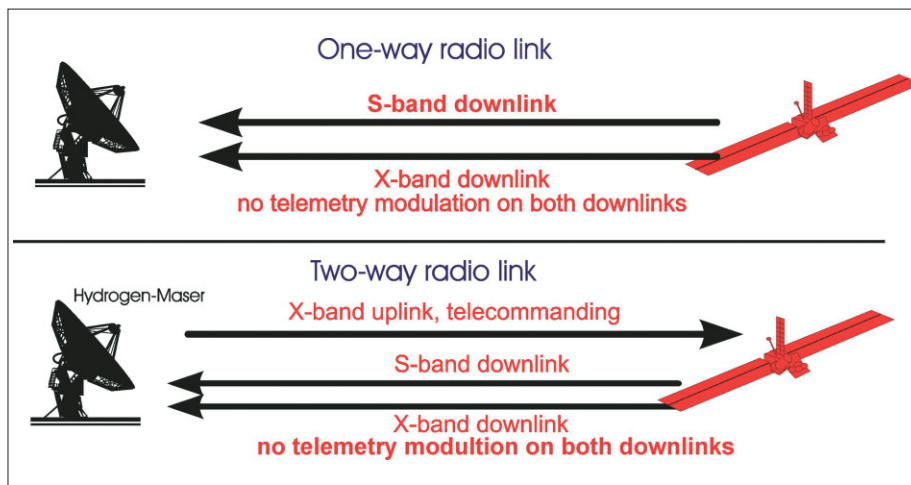


Fig. 12. Radio links between the Orbiter and the Earth station. Upper panel: one-way X-band and S-band downlink for bistatic radar. Lower panel: two-way radio link where the uplink is transponded phase-coherently with dual-frequency downlinks at X-band and S-band. Frequency stability is governed by a hydrogen maser at the ground station.

3.1 Mars Express radio subsystem

Mars Express can receive and transmit radio signals via either of two dedicated antenna systems:

- High Gain Antenna (HGA), a fixed parabolic dish of 1.60 m diameter, antenna gains 40 dBi and 28 dBi at X-band and S-band, respectively;
- two Low Gain Antennas (LGAs).

A block diagram of the characteristic features of the radio subsystem is shown in Fig. 10. Each of the two redundant transponders consist of an S-band and X-band receiver. The X-band transmitter output is amplified by a redundant 65 W Travelling Wave Tube Amplifier (TWTA) and the S-band downlink by a Solid State Amplifier of 5 W RF output. The spacecraft can receive and transmit at S-band (2.1 GHz) via the LGAs, or receive non-simultaneously at either X-band (7.1 GHz) or S-band via the HGA. The right-hand circular polarised downlink signals at S-band (2.3 GHz) and X-band (8.4 GHz) are transmitted via the HGA simultaneously (see an overview of frequencies in Table 1). The HGA (Fig. 11) is the primary antenna for receiving telecommands from and transmitting high rate telemetry in the operational phase. The LGAs are used during the commissioning phase and emergency operations.

MaRS uses two radio link modes (Fig. 12). The coherent two-way radio link is established by transmitting an uplink radio signal either at S-band or X-band to the spacecraft. A received S-band uplink carrier frequency is transponded to downlinks at S-band and X-band upon multiplication by the constant transponder ratios 240/221 and 880/221, respectively, in order to guarantee a ratio of the two downlinks of $880/240 = 11/3$. A received X-band uplink is multiplied by 880/749 and 240/749 to arrive at X-band and S-band downlink frequencies, respectively. Here again, the ratio of both frequencies is $880/240 = 11/3$. The two-way radio mode takes advantage of the superior frequency stability inherent to the hydrogen maser oscillator at the ground station on Earth. This mode is used for sounding the atmosphere and ionosphere, the gravity science applications and the sounding of the solar corona.

The one-way link mode is established by transmitting the X-band and S-band downlink simultaneously and phase coherently. It is used for the bistatic radar experiment.

3.2 Ground segment

Ground stations (Fig. 13) include antennas, associated equipment and operating systems in the tracking complexes of Perth, Australia (ESA, 35 m) and NASA's Deep Space Network (DSN, 34 m and 70 m) in California, Spain and Australia. A tracking

3. Technical Description

Table 1. Carrier frequencies.

	Uplink	Downlink	
S-band	2.1	2.3	GHz
X-band	7.1	8.4	GHz

Fig. 13. ESA and NASA ground station networks. The 15 m ESA antenna at Kourou will be used for the commissioning phase, while the new 35 m antenna near Perth will be the primary antenna. NASA will support specific mission phases and the radio science experiment with its Deep Space Network antennas at Goldstone (California), Canberra (Australia) and Madrid (Spain).

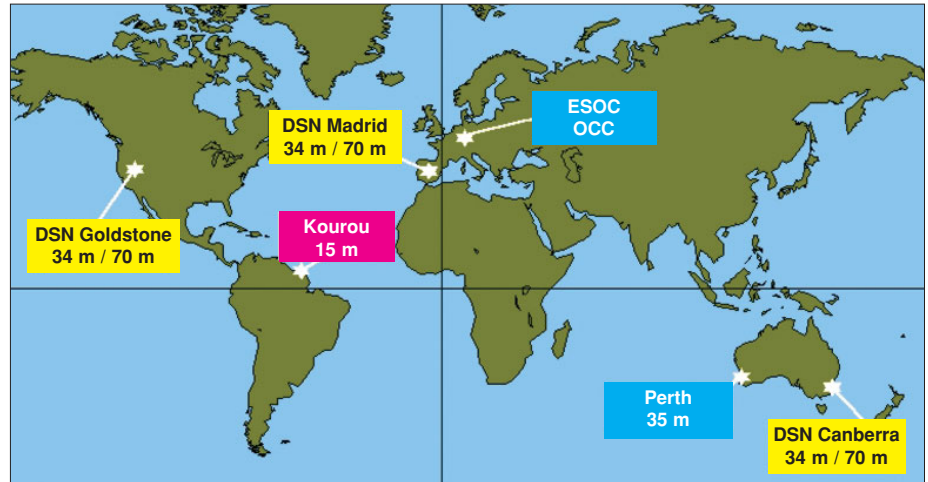


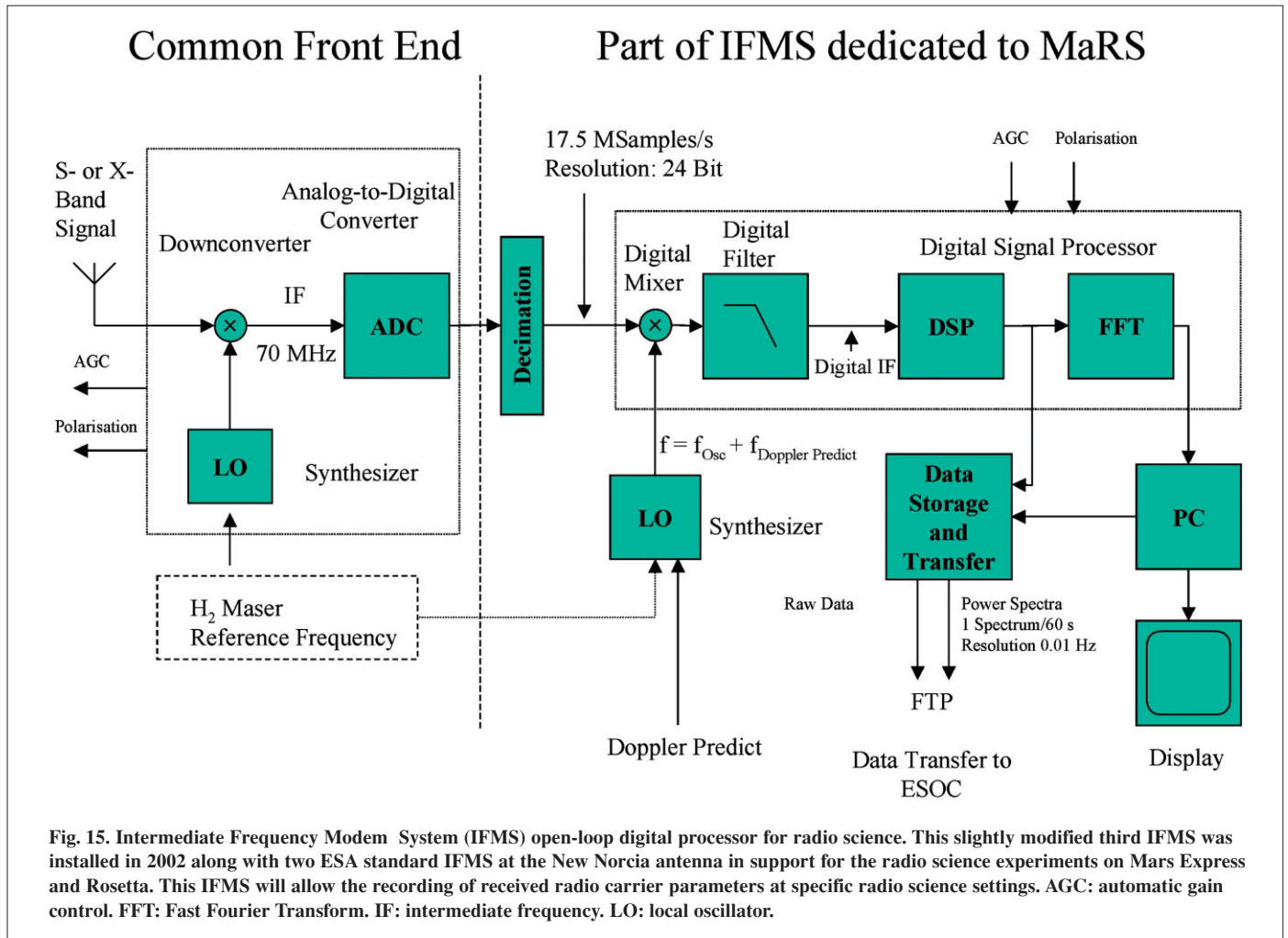
Fig. 14. ESA's new 35 m antenna at New Norcia, Australia.



pass consists of typically 8-10 h of spacecraft visibility and communication at the respective ground station site. Measurements of the spacecraft range and carrier Doppler shift can be obtained whenever the spacecraft is visible and its HGA is pointed towards Earth. The baseline calls for one communication pass at the ESA ground station per day, summarising approximately 1700 tracking passes for radio science (630 gravity passes, 750 occultations, 120 corona soundings, 200 bistatic radar observations). The use of the DSN antennas in California and Spain are under discussion and would usefully increase the number of tracking passes and experiment performance.

In the two-way mode, the ground station transmits an uplink radio signal at either S-band or at X-band and receives the dual-frequency downlink at X-band and S-band. Information about signal amplitude, received frequency and polarisation is extracted and stored as a function of ground receive time.

ESA's new 35 m ground station at New Norcia, Australia, about 200 km north of the older tracking complex in Perth, became operational in summer 2002 (Fig. 14). Its first deep space test with Ulysses was planned for September 2002. The station equipment consist of three identical new receiving systems designated as the Intermediate Frequency and Modem System (IFMS; Fig. 15). One is dedicated for radio science open-loop data recording of the Mars Express radio science



investigations and the Rosetta Radio Science Investigations experiment (Pätzold et al., 2000). This open-loop system will be used specifically for the radio sounding of the atmosphere/ionosphere, bistatic radar and solar corona investigations where closed-loop tracking receivers would typically lose lock. The IFMS operates on a 17.5 Msps 24-bit complex baseband stream (containing 12-bit words each for the *I* and *Q* channels) and resulting from filtering and decimating the 280 Msps 8-bit stream output data from the Common Front End Analogue-to-Digital Converter. These channels are provided for both RCP and LCP polarisations. The radio science raw data can be directly transferred to a mass storage device and/or processed by a Fast Fourier routine.

The DSN stations (Fig. 16) also provide uplinks at S-band or X-band. Dedicated radio science equipment functionally similar to the IFMS is available at all DSN stations (Asmar & Renzetti, 1993).

Radio science measurements in the ground stations can be done simultaneously on a non-interference basis with the transmission and/or reception of telecommands. However, since the signal-to-noise ratio of the carrier signal is considerably reduced when transmitting telemetry, a non-modulated downlink radio carrier is required in that case.

3.3 Observed quantities

The two data types (closed- and open-loop) can be generated simultaneously

Fig. 16. NASA's 70 m (foreground) and 34 m (background) deep space antennas at the Goldstone complex in the Mojave desert. (NASA)



regardless of the radio link configuration (one- or two-way). The received carrier frequencies, the signal strengths (received total power) and the polarisation of the radio signals are monitored at the ground station. Ground-based radiometric data are recorded using closed-loop receivers:

- amplitude and phase (Doppler) measurements (two- and one-way modes);
- ranging measurements (two-way mode only);
- full polarisation measurements (primarily one-way mode).

3.3.1 Doppler shift

The transmission of dual-frequency phase-coherent downlinks at S-band and X-band with the constant ratio of 11/3 makes it feasible to separate the dispersive from the non-dispersive Doppler effects on the radio link.

The frequency of the radio carrier is shifted according to the relative radial velocity between the transmitter and the receiver (classical Doppler shift). Furthermore, a relative phase shift is experienced when the radio wave propagates through an ionised medium (ionosphere, interplanetary medium, solar corona). Excluding oscillator drifts and instabilities, the frequency shift for a one-way (spacecraft-to-Earth) radio link due to plasma is:

$$\Delta f = f - f_0 = -\frac{f_0}{c} \frac{ds}{dt} + \frac{40.31}{c} \frac{1}{f_0} \frac{d}{dt} \int_{s/c}^{Earth} N_e ds \quad (1)$$

where ds/dt is the rate of change of the distance between transmitter and receiver (relative velocity), c is the speed of light and f_0 is the carrier frequency. The integral of the electron density $N_e(s)$ along the propagation path ds of the radio wave from the spacecraft (s/c) to Earth is also called the columnar electron content, or column density.

The first term on the right hand side of (1) is the classical Doppler shift (linear in f_0) and the second term is the dispersive propagation effect of radio waves in ionised media, which is inversely proportional to f_0 . A larger classical Doppler shift is measured on the X-band, but the lower S-band frequency is more sensitive to dispersive frequency shifts. A change in relative velocity of 2 cm s^{-1} yields a classical Doppler frequency shift of 0.6 Hz at X-band. A dispersive frequency shift of 0.6 Hz at S-band is produced by a change in electron content by one hexem (10^{16} electrons m^{-2}) within 1 s.

It is not possible to separate classical and dispersive frequency shifts from the observed total change in frequency Δf at either f_s or f_x , the S-band or X-band carrier frequency, respectively, alone. However, using Eq. 1 for the two phase-coherent downlinks at X-band and S-band with a constant transponder ratio of $880/240 = 11/3$ and calculating the differential Doppler

$$\Delta f_s - \frac{3}{11} \Delta f_x, \quad (2)$$

where Δf_s and Δf_x are the observed Doppler shifts at S-band and X-band, respectively. According to Eq. 1, it is possible to isolate the dispersive frequency shift:

$$\begin{aligned} \Delta f_s - \frac{3}{11} \Delta f_x &= -\frac{\frac{d}{dt} s}{c} f_s + \frac{40.31}{c} \frac{1}{f_s} \frac{d}{dt} \int_{s/c}^{Earth} N ds + \frac{3}{11} \frac{\frac{d}{dt} s}{c} f_x - \frac{3}{11} \frac{40.31}{c} \frac{1}{f_x} \frac{d}{dt} \int_{s/c}^{Earth} N ds \\ &= \frac{40.31}{c} f_s \left(\frac{1}{f_s^2} - \frac{1}{f_x^2} \right) \frac{d}{dt} \int_{s/c}^{Earth} N ds \end{aligned} \quad (3)$$

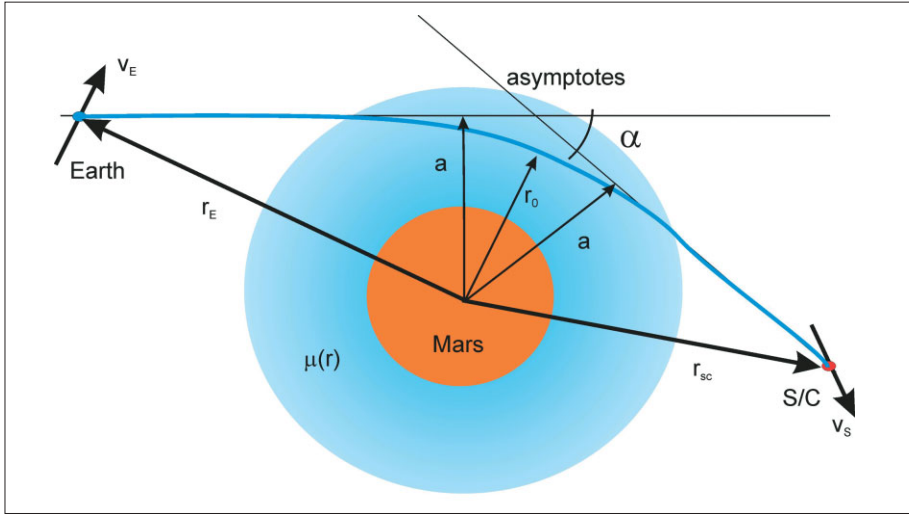


Fig. 17. Radio ray bending in a planetary atmosphere. Refractivity is represented as a function of radius. The bending can be described by the total bending angle α , and the distance of the ray asymptotes, a . In a spherically symmetric atmosphere, the radio path remains in a plane and bends about the centre of the system. The closest approach distance of the bended ray is r_{01} . The plane is defined by the geometry of the constellation (distance to Earth vector, velocity vector of Earth, distance vector to spacecraft, velocity vector of spacecraft with respect to Mars).

The ‘differential Doppler effect’ (Eq. 3), calculated from the observed frequency shifts, is used to determine the changes in electron content. All oscillator drifts and relative velocities are eliminated in this process. This result can further be used to correct each single classical frequency shift for the dispersive propagation effects .

The example above was derived for a one-way link. It can be shown that the calculation of the differential Doppler of a two-way radio link, when the spacecraft transmitted carrier frequencies are derived coherently from the received (and Doppler-shifted) uplink frequency, leads to exactly the same relation. In either case, Eq. 3 can be used to determine the electron content along the downlink path. Integration of Eq. 3 with respect to time yields the differential phase, which is proportional to changes in electron content along the downlink from the beginning of the tracking pass.

3.3.2 Ranging (propagation delay)

The absolute value of total electron content can be determined from the differential propagation delay by two-way ranging at S-band and X-band:

$$\tau_s - \tau_x = \frac{40.31}{c} \left(\frac{1}{f_s^2} - \frac{1}{f_x^2} \right) \int_{s/c}^{Earth} N ds \quad (4)$$

Typically, the Doppler or phase measurements are more sensitive than the ranging measurements by about two orders of magnitude (Bird, 1982).

3.3.3 Ray bending in atmospheres

Radio occultation studies of atmospheres can be understood in terms of ‘geometric’ or ‘ray’ optics refraction of signals travelling between spacecraft and ground stations. In a spatially varying medium where the wavelength is very short compared with the scale of variation in refractive index, the direction of propagation of an electromagnetic wave always curves in the direction of increasing refractivity. Consequently, in a spherically symmetric atmosphere with gas refractivity proportional to number density constantly decreasing with height, the radio path remains in a plane and bends about the centre of the system. The degree of bending depends on the strength of the refractivity gradient. This simple model approximates a real atmosphere and is useful for understanding the basic phenomena of radio occultation (Fjeldbo, 1964).

The geometry is illustrated in Fig. 17, where the atmosphere is represented by the

Table 2. Doppler velocity error σ_v (mm s⁻¹) for 1 s integration time.

	0.8 AU		2.5 AU	
	S-band	X-band	S-band	X-band
Thermal noise (ground station)	0.9	0.01	2.00	0.03
Transponder phase noise	0.42	0.26	0.42	0.26
Total error (two-way coherent mode)	0.99	0.26	2.04	0.26

refractivity as a function of radius from the centre, $\mu(r_0)$, and the bending can be described in terms of a total bending angle, α , and a ray asymptote, a . The variation of the bending angle, ray asymptote and refractivity are linked through an Abel transform (Fjeldbo & Eshleman, 1964),

$$\alpha(a) = -2a \int_{r=r_0}^{\infty} \frac{1}{\mu} \frac{\partial \mu}{\partial r} \frac{\partial r}{\sqrt{(\mu r)^2 - a^2}} \quad (5)$$

where $r_0 = \frac{a}{\mu(r_0)}$ is the ray periapse and,

$$\mu(r_{01}) = \exp \left\{ -\frac{1}{\pi} \int_{a=a_1}^{a=\infty} \ln \left\{ \frac{a}{a_1} + \sqrt{\left(\frac{a}{a_1}\right)^2 - 1} \right\} \frac{d\alpha}{da} da \right\} \quad (6)$$

with $r_0 = \frac{a}{\mu(r_{01})}$.

In this last expression, a_1 represents the asymptotic miss distance for a ray whose radius of closest approach is r_{01} . Thus, for spherical atmospheres, if $\alpha(a)$ is known, then the corresponding refractivity profile can be found exactly. For non-spherical geometry, alternative numerical solutions are available. The bending angle and the ray asymptote can be determined accurately by radio occultation to create an experimentally derived table of α versus a , or $\alpha(a)$.

In order to interpret the refractivity in terms of gas parameters, the pressure and temperature are calculated assuming hydrostatic equilibrium, for example, from

$$p(h) = \langle m \rangle \int_h^{\infty} g(h) N(h) dh \quad (7)$$

and

$$T(h) = \frac{p(h)}{k_B N(h)} \quad (8)$$

where $p(h)$ and $T(h)$ are the pressure and temperature as a function of height h , respectively, g is the acceleration of gravity, k_B is Boltzmann's constant, $\langle m \rangle$ is the mean molecular mass, and $N(h)$ is the molecular number density. Formal use of these equations requires *a priori* knowledge of the atmospheric composition.

3.4 Error budget

The major noise sources contributing to the Doppler velocity error are the thermal noise of the radio receiver on the ground for one-way observations, and both on the ground and aboard the spacecraft for two-way observations. The velocity error σ_v contributed by the ground station is given by

$$\sigma_v = \frac{c}{4\pi f \Delta t} \sqrt{\frac{2BN_0}{C}} \quad (9)$$

and the transponder phase noise σ_ϕ by

$$\sigma_v = \frac{c \sqrt{2}}{4\pi f t} \sigma_\phi \quad (10)$$

where B is the receiver bandwidth, C and N_0 are the received carrier power and the noise power density, respectively. The transponder phase noise σ_ϕ was experimentally determined by Remus et al. (2001) with a transponder electrical qualification model on ground. The total velocity error σ_v is calculated in Table 2 for an integration time Δt of 1 s at S-band and X-band.

Typical integration times for practical observations are in the range 1-10 s, thus yielding 0.26-0.03 mm s⁻¹ Doppler error, respectively, at X-band for 0.8 AU, large solar elongation angles and quiet solar wind conditions. The sensitivity in the electron content from differential Doppler measurements (Eq. 2) at 1 s integration time is computed to be in the order of 0.02 hexem s⁻¹.

- Acuna, M.H., Connerney, J.E.P., Wasilewski, P., Lin, R.P., Anderson, K.A., Carlson, C.W., McFadden, J., Curtis, D.W., Mitchell, D., Reme, H., Mazelle, C., Sauvaud, J.A., D'Uston, C., Cros, A., Medale, J.L., Bauer, S.J., Cloutier, P., Mayhew, M., Winterhalter, D. & Ness, N.F. (1998). Magnetic Field and Plasma Observations at Mars: Initial Results of the Mars Global Surveyor Mission. *Science* **279**, 1676-1680.
- Anderson, J.D., Colombo, G., Esposito, P.B., Lau, E.L. & Trager, G.B. (1987). The Mass, Gravity Field, and Ephemeris of Mercury. *Icarus* **71**, 337-349.
- Anderson, J.D., Armstrong, J.W., Campbell, J.K., Eastabrook, F.B., Krisher, T.P. & Lau, E.L. (1992). Gravitation and Celestial Mechanics Investigations with Galileo. *Space Sci. Rev.* **60**, 591-610.
- Anderson, J.D., Lau, E.L., Sjogren, W.L., Schubert, G. & Moore, W.B. (1997). Europa's Differentiated Internal Structure: Inferences from Two Galileo Encounters. *Science* **176**, 1236-1239.
- Asmar, S.W. & Renzetti, N.A. (1993). The Deep Space Network as an Instrument for Radio Science Research. *JPL Publication 80-93, Rev. 1*.
- Barth, C.A., Stewart, A.I.F., Bougher, S.W., Hunten, D.M., Bauer, S.J. & Nagy, A.F. (1992). Aeronomy of the Current Martian Atmosphere. In *Mars* (Eds. H.H. Kieffer, B.M. Jakosky, C.W. Snyder, M.S. Matthews), University of Arizona Press, Tucson, USA, pp1054-1089.
- Bird, M.K. (1982). Coronal Investigations with Occulted Spacecraft Signals. *Space Sci. Rev.* **33**, 99-126.
- Bird, M., Asmar, S.W., Brenkle, J.P., Edenhofer, P., Paetzold, M. & Volland, H. (1992). The Coronal Sounding Experiment. *Astron. Astrophys. Suppl. Ser.* **92**, 425-430.
- Bird, M.K., Volland, H., Pätzold, M., Edenhofer, P., Asmar, S.W. & Brenkle, J.P.

References

- (1994). The Coronal Electron Density Distribution Determined from Dual-Frequency Ranging Measurements during the 1991 Solar Conjunction of the Ulysses Spacecraft. *Astrophys. J.* **426**, 373-381.
- Bird, M.K., Allison, M., Asmar, S.W., Atkinson, D.H., Edenhofer, P., Heyl, M., Iess, L., Plettemeier, D., Tyler, G.L. & Wohlmuth, R. (1995). The Huygens Doppler Wind Experiment. In *Huygens: Science, Payload and Mission* (Ed. A. Wilson), ESA SP-1177, European Space Agency, pp139-162.
- Bird, M.K., Paetzold, M., Edenhofer, P., Asmar, S.W. & McElrath, T.P. (1996). Coronal Radio Sounding with Ulysses: Solar Wind Electron Density near 0.1 AU during the 1995 Conjunction. *Astron. Astrophys.* **316**, 437-448.
- Edgett, K.S., Butler, B.J., Zimbelman, J.R. & Hamilton, V.E. (1997). Geologic Context of the Mars Radar 'Stealth' Region in Southwestern Tharsis. *J. Geophys. Res.* **102**, 21545-21567.
- Eshleman, V.R., Tyler, G.L., Anderson, J.D., Fjeldbo, G., Levy, G.S., Wood, G.E. & Croft, T.A. (1977). Radio Science Investigations with Voyager. *Space Sci. Rev.* **21**(2), 207-232.
- Eshleman, V.R. (1973). The Radio Occultation Method for the Study of Planetary Atmospheres. *Planet. Space Sci.* **21**, 1521-1531.
- Eshleman, V.R. (1987). The Radar-Glory Theory for Icy Moons with Implications for Radar Mapping. *Adv. Space Res.* **7**, 133-136.
- Fjeldbo, G. (1964). Bistatic Radar Methods for Studying Planetary Ionospheres and Surfaces. Stanford Electronics Laboratory, Stanford University, SU-SEL-64-025.
- Fjeldbo, G. & Eshleman, V.R. (1968). The Atmosphere of Mars Analyzed by Integral Inversion of the Mariner IV Occultation Data. *Planet. Space Sci.* **16**, 1035-1059.
- Gresh, D.L., Marouf, E.A., Tyler, G.L., Rosen, P.A. & Simpson, R.A. (1989). Voyager Radio Occultation by Uranus' Rings. *Icarus* **78**, 131-168.
- Hagfors, T., Gold, T. & Ierke, H.M. (1985). Refraction Scattering as Origin of the Anomalous Radar Returns of Jupiter's Satellites. *Nature* **315**, 637-640.
- Hapke, B. (1990). Coherent Backscattering and the Radar Characteristics of the Outer Planet Satellites. *Icarus* **88**, 407-417.
- Hinson, D.P., Simpson, R.A., Twicken, J.D., Tyler, G.L. & Flasar, F.M. (1999). Initial Results from Radio Occultation Measurements with Mars Global Surveyor. *J. Geophys. Res.* **104** (E11), 29997-27012.
- Hinson, D.P., Tyler, G.L., Hollingworth, J.L. & Wilson, R.J. (2001). Radio Occultation Measurements of Forced Atmospheric Waves on Mars. *J. Geophys. Res.* **106** (E1), 1463-1480.
- Howard, H.T., Eshleman, V.R., Hinson, D.P., Kliore, A.J., Lindal, G.F., Woo, R., Bird, M.K., Volland, H., Edenhofer, P., Pätzold, M. & Porsche, H. (1992). Galileo Radio Science Investigations. *Space Sci. Rev.* **60**, 565-590.
- Janle, P. & Erkul, E. (1991). Gravity Studies of the Tharsis Area on Mars. *Earth, Moon & Plan.* **53**, 217-232.
- Janle, P. & Janssen, D. (1986). Isostatic Gravity and Elastic Bending Models of Olympus Mons, Mars. *Ann. Geophysicae* **4**, B, 537-546.
- Karayel, E.T. & Hinson, D.P. (1997). Sub-Fresnel-scale Vertical Resolution in Atmospheric Profiles from Radio Occultation. *Radio Sci.* **32**, 411-423.
- Karl, J., Pätzold, M. & Bird, M.K. (1997). Coronal Radio Sounding: Non-Gaussian Turbulence in the Source Regions of the Solar Wind. *Geophys. Res. Lett.* **24**, 2881-2884.
- Kliore, A.J. (1992). Radio Occultation Observations of the Ionospheres of Mars and Venus. In *Venus and Mars: Atmospheres, Ionospheres, and Solar Wind Interaction* (Eds. J.G. Luhmann, M. Tatrallyay & R.O. Pepin), *Geophys. Monograph* **66**, 265-276.
- Kliore, A.J. & Luhmann, J.G. (1991). Solar Cycle Effects on the Structure of the Electron Density Profiles in the Dayside Ionosphere of Venus. *J. Geophys. Res.* **96**, 21281-21289.
- Kliore, A.K., Cain, D.L., Levy, G.S., Eshleman, V.R., Fjeldbo, G. & Drake, F.D.

- (1965). Occultation Experiment: Results of the First Direct Measurement of Mars' Atmosphere and Ionosphere. *Science* **149**, 1243-1248.
- Kliore, A.J., Anderson, J.D., Armstrong, J.W., Asmar, S.W., Hamilton, C.L., Rappaport, N.J., Walquist, H.D., Ambrosini, R., Bertotti, B., Flasar, F.M., French, R.G., Iess, L., Marouf, E.A. & Nagy, A.F. (2002). Cassini Radio Science. *Space Sci. Rev.*, in Press.
- Kolosov, M.A., Yakovlev, O.I., Efimov, A.I., Pavelyev, A.G. & Matyugov, S.S. (1979). Radio Occultation of the Venusian Atmosphere and Bistatic Radar Location of the Surface of Venus using the Venera-9 and Venera-10 Satellites. *Radio Sci.* **14**, 163-173.
- Konopliv, A.S. & Sjogren, W.L. (1995). The JPL Mars Gravity Field, Mars50c, Based upon Viking and Mariner 9 Doppler Tracking Data. *JPL Publication* **95-5**.
- Marouf, E.A., Tyler, G.L. & Rosen, P.A. (1986). Profiling Saturn's Rings by Radio Occultation. *Icarus* **68**, 120-166.
- Muhleman, D.O., Butler, B.J., Grossman, A.W. & Slade, M.A. (1991). Radar Images of Mars. *Science* **253**, 1508-1513.
- Nozette, S., Lichtenberg, C.L., Spudis, P., Bonner, R., Ort, W., Malaret, E., Robinson, M. & Shoemaker, E. (1996). The Clementine Bistatic Radar Experiment. *Science* **274**, 1495-1498.
- Nozette, S. (2001). Spudis, P.D., Robinson, M.S., Bussey, D.B.J., Lichtenberg, C. & Bonner, R. Integration of Lunar Polar Remote-Sensing Data Sets: Evidence for Ice at the Lunar South Pole. *J. Geophys. Res.* **106** (E10), 23253-23266.
- Pätzold, M., Bird, M.K., Volland, H., Edenhofer, P. & Buschert, H.. (1991a). Dynamics of the Giotto Spacecraft in the Inner Dust Coma of Comet P/Halley; Part 1: Observations. *Z. Flugwiss. Weltraumforsch* **15**, 89-96.
- Pätzold, M., Bird, M.K., Volland, H., Edenhofer, P. & Buschert, H. (1991b). Dynamics of the Giotto Spacecraft in the Inner Dust Coma of Comet P/Halley; Part 2: Interpretations. *Z. Flugwiss. Weltraumforsch* **15**, 159-164.
- Pätzold, M., Bird, M.K. & Edenhofer, P. (1993). The Change of Giotto's Dynamical State during the P/Grigg-Skjellerup Flyby Caused by Dust Particle Impacts. *J. Geophys. Res.* **98**, A12, 20911-20920.
- Pätzold, M., Bird, M.K., Edenhofer, P., Asmar, S.W. & McElrath, T.P. (1995). Dual-frequency Radio Sounding of the Solar Corona during the 1995 Conjunction of the Ulysses Spacecraft. *Geophys. Res. Lett.* **22**, 3313-3316.
- Pätzold, M., Karl, J. & Bird, M.K. (1996). Coronal Sounding with Ulysses: Phase Scintillation Spectra in Coronal Holes and Streamers. *Astron. Astrophys.* **316**, 449-456.
- Pätzold, M., Tsurutani, B.T. & Bird, M.K., (1997). An Estimate of Large-scale Solar Wind Density and Velocity Profiles in a Coronal Hole and the Coronal Streamer Belt. *J. Geophys. Res.* **102**, 24151-24160.
- Pätzold, M., Neubauer, F.M., Wennmacher, A., Aksnes, K., Anderson, J.D., Asmar, S.W., Tinto, M., Tsurutani, B.T., Yeomans, D.K., Barriot, J.-P., Bird, M.K., Boehnhardt, H., Gill, E., Montenbruck, O., Grun, E., Hausler, B., Ip, W.H., Thomas, N., Marouf, E.A., Rickman, H., Wallis, M.K. & Wickramasinghe, N.C. (2000). Rosetta Radio Science Investigations (RSI). *Research Notes #4*, Institut für Geophysik und Meteorologie, Universität zu Köln.
- Pätzold, M., Wennmacher, A., Häusler, B., Eidel, W., Morley, T., Thomas, N. & Anderson, J.D. (2001). Mass and Density Determinations of 140 Siwa and 4979 Otawara during the Rosetta Flybys. *Astron. Astrophys.* **370**, 1122-1127.
- Peters, K.J. (1992). The Coherent Backscatter Effect: a Vector Formulation Accounting for Polarization and Absorption Effects and Small or Large Scatterers. *Physical Review B* **46**, 801-812.
- Pettengill, G.H., Ford, P.G. & Simpson, R.A. (1996). Electrical Properties of the Venus Surface from Bistatic Radar Observations. *Science* **272**, 1628-1631.
- Pettengill, G.H., Campbell, B.A., Campbell, D.B. & Simpson, R.A. (1997). Surface Scattering and Dielectric Properties. In *Venus II* (Eds. S.W. Bougher, D.M. Hunten & R.J. Phillips), Tucson, University of Arizona Press, USA, p527.

- Remus, S., Häusler, B., Pätzold, M. & Wennmacher, A. (2001). Ergebnisse der Radio Science Testmessungen an den ESA Satelliten Rosetta und Mars Express. Deutscher Luft- und Raumfahrtkongress, 17-20 September 2001, DGLR-2001-022.
- Simpson, R.A. & Tyler, G.L. (1981). Viking Bistatic Radar Experiment: Summary of First-order Results Emphasizing North Polar Data. *Icarus* **46**, 361-389.
- Simpson, R.A., Tyler, G.L. & Schaber, G.G. (1984). Viking Bistatic Radar Experiment: Summary of Results in Near-equatorial Regions. *J. Geophys. Res.* **89**, 10385-10404.
- Simpson, R.A. (1993). Spacecraft Studies of Planetary Surfaces using Bistatic Radar. *IEEE Transactions on Geoscience and Remote Sensing* **31**, 465-482.
- Simpson, R.A. & Tyler, G.L. (1999). Reanalysis of Clementine Bistatic Radar from the Lunar South Pole. *J. Geophys. Res.* **104**, 3845-3862.
- Smith, D.E., Lerch, F.J., Nerem, R.S., Zuber, M.T., Patel, G.B., Fricke, S.K. & Lemoine, F.G. (1993). An Improved Gravity Model for Mars: Goddard Mars Model 1. *J. Geophys. Res.* **98**, 20871-20889.
- Smith, D.E., Sjogren, W.L., Tyler, G.L., Balmino, G., Lemoine, F.G. & Konopliv, A.S. (1999). The Gravity Field of Mars: Results from Mars Global Surveyor. *Science* **286**, 94-97.
- Standish, E.M. (1993). Planet X – No Dynamical Evidence in the Optical Observations. *Astron. J.* **105**(5), 2000-2006.
- Tyler, G.L. (1968a). Oblique-scattering Radar Reflectivity of the Lunar Surface: Preliminary Results from Explorer 35. *J. Geophys. Res.* **73**, 7609-7620.
- Tyler, G.L. (1968b). Brewster Angle of the Lunar Crust. *Nature* **219**, 1243-1244.
- Tyler, G.L. (1987). Radio Propagation Experiments in the Outer Solar System with Voyager. *Proc. IEEE* **75**, No.10, 1404-1431.
- Tyler, G.L. & Howard, H.T. (1973). Dual-frequency Bistatic Radar Investigations of the Moon with Apollos 14 and 15. *J. Geophys. Res.* **78**, 4852-4874.
- Tyler, G.L., Balmino, G., Hinson, D.P., Sjogren, W.L., Smith, D.E., Simpson, R.A., Asmar, S.W., Priest, P. & Twicken, J.D. (2001). Radio Science Observations with Mars Global Surveyor: Orbit Insertion through one Mars year in Mapping Orbit. *J. Geophys. Res.* **106**, E10, 23327-23348.
- Tyler, G.L., Balmino, G., Hinson, D.P., Sjogren, W.L., Smith, D.E., Woo, R., Asmar, S.W., Conally, M.J., Hamilton, C.L. & Simpson, R.A. (1992). Radio Science Investigations with Mars Observer. *J. Geophys. Res.* **97**, 7759-7779.
- Tyler, G.L., Brenkle, J.P., Komarek, T.A. & Zygielbaum, A.I. (1977). The Viking Solar Corona Experiment. *J. Geophys. Res.* **82**, 4335-4340.
- Tyler, G.L., Eshleman, V.R., Fjeldbo, G., Howard, H.T. & Peterson, A.M. (1967). Bistatic-radar Detection of Lunar Scattering Centers with Lunar Orbiter I. *Science* **157**, No. 3785, 193-195.
- Tyler, G.L., Eshleman, V.R., Hinson, D.P., Marouf, E.A., Simpson, R.A., Sweetnam, D.N., Anderson, J.D., Campbell, J.K., Levy, G.S. & Lindal, G.F. (1989). Voyager Radio Science Observations of Neptune and Triton. *Science* **246**, 1466-1473.
- Tyler, G.L., Ford, P.G., Campbell, D.B., Elachi, C., Pettengill, G.H. & Simpson, R.A. (1991). Magellan – Electrical and Physical Properties of Venus' Surface. *Science* **252**, 265-270.
- Wohlmut, R., Plettmeier, D., Edenhofer, P., Bird, M.K., Pätzold, M. & Asmar, S.W. (1997). Measurement of the Propagation Speed of Plasma Inhomogeneities in the Solar Corona using an Uplink/Downlink Cross-correlation Method. *Radio Sci.* **32**, 617-628.
- Yakovlev, O.I. & Efimov, A.I. (1966). Studies of Reflection of Meter-length Radio Waves. *Dokladi Akademii Nauk SSSR* **174**, 583-584.
- Yeomans, D.K., Antreasian, P.G., Barriot, J.-P., Chesley, S.R., Dunham, D.W., Farquhar, R.W., Giorgini, J.D., Helfrich, C.E., Konopliv, A.S., McAdams, J.V., Miller, J.K., Owen, W.M., Scheeres, D.J., Thomas, P.C., Veverka, J. & Williams, B.G. (2000). Radio Science Results during the NEAR-Shoemaker Spacecraft Rendezvous with Eros. *Science* **289**, 2085-2088.

- Yeomans, D.K., Barriot, J.-P., Dunham, D.W., Farquhar, R.W., Giorgini, J.D., Helfrich, C.E., Konopliv, A.S., McAdams, J.V., Miller, J.K., Owen, W., Jr., Scheeres, D.J., Synnott, S.P. & Williams, B.G. (1997). Estimating the Mass of Asteroid 253 Mathilde from Tracking Data during the NEAR Flyby. *Science* **278**, 2106-2109.
- Yuan, D.-N., Sjogren, W.L., Konopliv, A.S. & Kucinskas, A.B. (2001). Gravity Field of Mars: A 75th Degree and Order Model. *J. Geophys. Res.* **106**, E10, 23377-23402.

Acknowledgements

The Mars Express Orbiter Radio Science (MaRS) experiment is funded by the Deutsches Zentrum für Luft- und Raumfahrt (DLR), Bonn, Germany, and the National Aeronautics and Space Administration (NASA), Washington DC, USA.